Mechanics of Advanced Materials and Structures

ISSN: (Print) (Online) Journal homepage: https://www.tandfonline.com/loi/umcm20

Systematic calibration procedure for CFRP sheets and rods strengthened RC T-beams by using RBSM

Joko Purnomo, Aylie Han, Rito Yamakawa & Buntara S. Gan

To cite this article: Joko Purnomo, Aylie Han, Rito Yamakawa & Buntara S. Gan (2022): Systematic calibration procedure for CFRP sheets and rods strengthened RC T-beams by using RBSM, Mechanics of Advanced Materials and Structures, DOI: 10.1080/15376494.2022.2111483

To link to this article: https://doi.org/10.1080/15376494.2022.2111483

Published online: 22 Aug 2022.

Submit your article to this journal

View related articles

View Crossmark data

Full Terms & Conditions of access and use can be found at
https://www.tandfonline.com/action/journalInformation?journalCode=umcm20

MECHANICS OF ADVANCED MATERIALS AND STRUCTURES
https://doi.org/10.1080/15376494.2022.2111483

Taylor & Francis
Taylor & Francis Group

ORIGINAL ARTICLE

Check for updates

Systematic calibration procedure for CFRP sheets and rods strengthened RC T-beams by using RBSM

Joko Purnomo[a,b], Aylie Han[a,c], Rito Yamakawa[d], and Buntara S. Gan[e]

[a]Department of Civil Engineering, Diponegoro University, Semarang, Indonesia; [b]Department of Civil Engineering, Petra Christian University, Surabaya, Indonesia; [c]World Class Research Program, Universitas Diponegoro, Semarang, Indonesia; [d]Department of Architecture, Graduate School of Engineering, Nihon University, Koriyama, Japan; [e]Department of Architecture, College of Engineering, Nihon University, Koriyama, Japan

ABSTRACT

In this study, a nonlinear 2D rigid body spring model (RBSM) was developed to verify the experimental works of Carbon Fiber Reinforced Polymer (CFRP) sheets and rods strengthened reinforced concrete (RC) T-shape beam (RC T-beam) section under a combination of bending and shearing loads. Modified Mohr–Coulomb criteria were adopted for modeling the plastic damage of concrete material. The orthotropic smeared layers representing the steel and CFRP materials were laminated on the concrete surface to model the reinforcing steel bars, stirrup steel, and CFRP sheets and rods. A mechanical behavior-based approach to fit the experimental results was discussed using the numerical results at each calibration stage. This study shows how the gradient of compressive and ultimate tensile strength of concrete affects the initial flexure behavior of the load-displacement curve of an RC T-beam. In contrast with finite element modeling, the RBSM can exhibit the crack propagation processes of element separation during the simulation. The calibrations showed the agreement of the models used in predicting the flexural behavior, ultimate load, and strengthening effects of the CFRP sheets and rods to the RC T-beam under bending loads. A systematic calibration procedure combined with the recommended use of energy-based criteria to evaluate the results of calibrated load-displacement curve was proposed.

ARTICLE HISTORY
Received 14 April 2022
Accepted 5 August 2022

KEYWORDS
Calibration, CFRP, strengthening, experiment, RBSM

1. Introduction

Recent significant earthquakes were used to drive the revision and modification of structural earthquake design codes, such as updates in regional earthquake mapping, response spectra, and strength criteria. The latest revisions and modifications require increasing the ultimate load capacity of steel-reinforced concrete (RC) structures under earthquake loading. To cope with the latest provision, it is more economical to design a strengthening method considering a combination of high shearing force and high bending moment. Without earthquake loading, the gravitational self-weight of a structural member raises the bending moment and shear force along the length of a beam (Figure 1(a)). Figure 1(b) shows the distribution of the bending moment and shear force along the same beam when subjected to an earthquake loading. When the superposition of the self-weight and horizontal inertial forces due to an earthquake are summed, the bending moment and shear force distributions increase at the joint of beam and column (Figure 1(c)).

During an earthquake, the most significant bending moment and shear force combination are found at the joint of beam and column (Figure 2(a)). Because the beam and slab are cast simultaneously during the construction phase, design codes require that the floor slab be considered the flange of a monolithic T-beam (Figure 2(b)). At the joint of beam and column, a negative bending moment makes the stress state of the flange of the T-beam in tension. Most of the stresses in the web portion of the T-beam are compressive due to the negative bending moment. At the same time, the T-beam also bears the most significant shear force at the joint.

To conduct an experiment on an asymmetric monolith RC T-beam requires careful consideration of the loading conditions. Applying the load on the flange part (slab) causes an undesirable lateral buckling phenomenon to the beam specimen. Therefore, the load was applied downward from the web part (beam) of the monolithic RC T-beam to observe the most significant combination of bending moment and shear force at the mid-span of the beam. Moreover, to do the experiment using conventional testing facility, the beam specimen has to be rotated 180 degrees (Figure 2(c)).

One of the most popular strengthening methods for existing structure element members is the use of Carbon Fiber Reinforced Polymer (CFRP) materials [1–9]. The variation of using glass instead of carbon material can be found in the work of Dutta et al. [10]. CFRP materials have the most considerable advantage among other strengthening methods, especially for strengthening existing structures [11–13]. It

CONTACT Buntara S. Gan gan.buntarasthenly@nihon-u.ac.jp Departement of Architecture, College of Engineering, Nihon University, Koriyama, Japan.
© 2022 Taylor & Francis Group, LLC

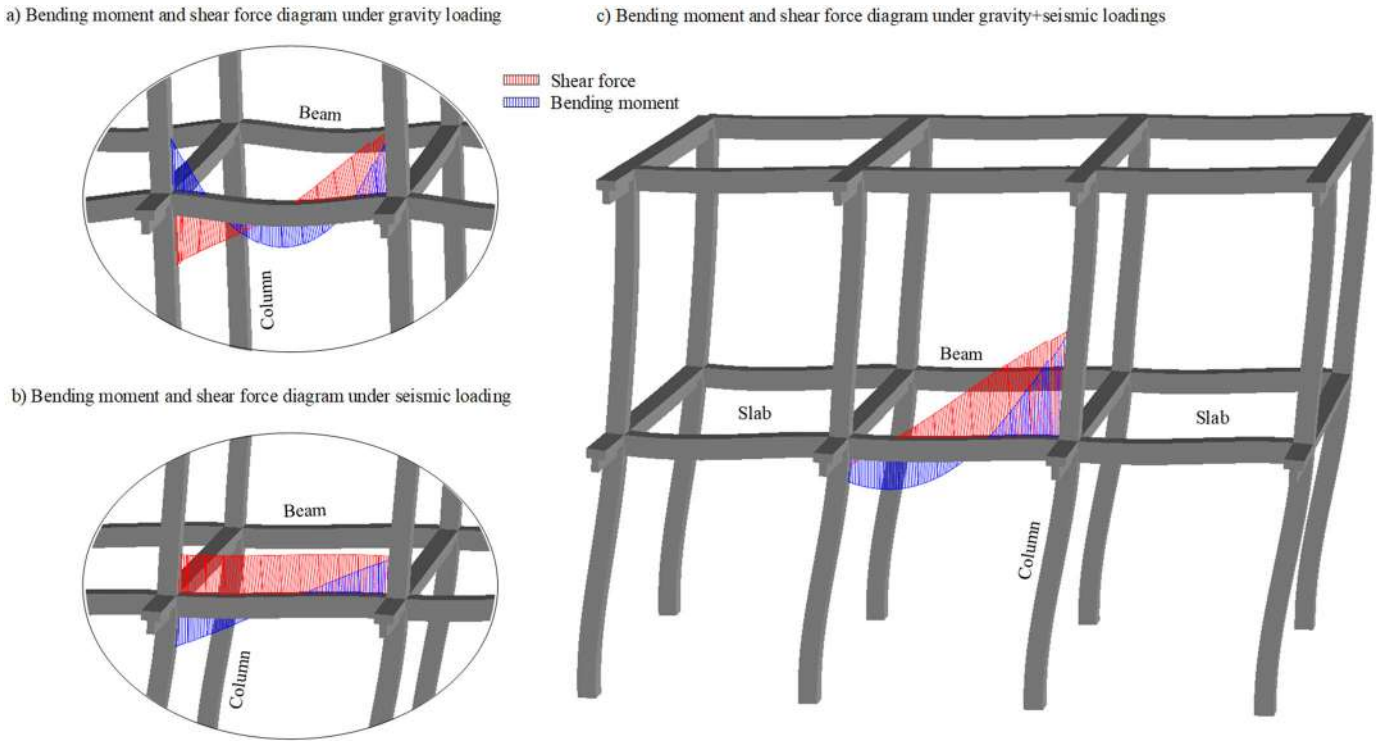

Figure 1. Superposition of the bending moment and shear stress during an earthquake (schematic).

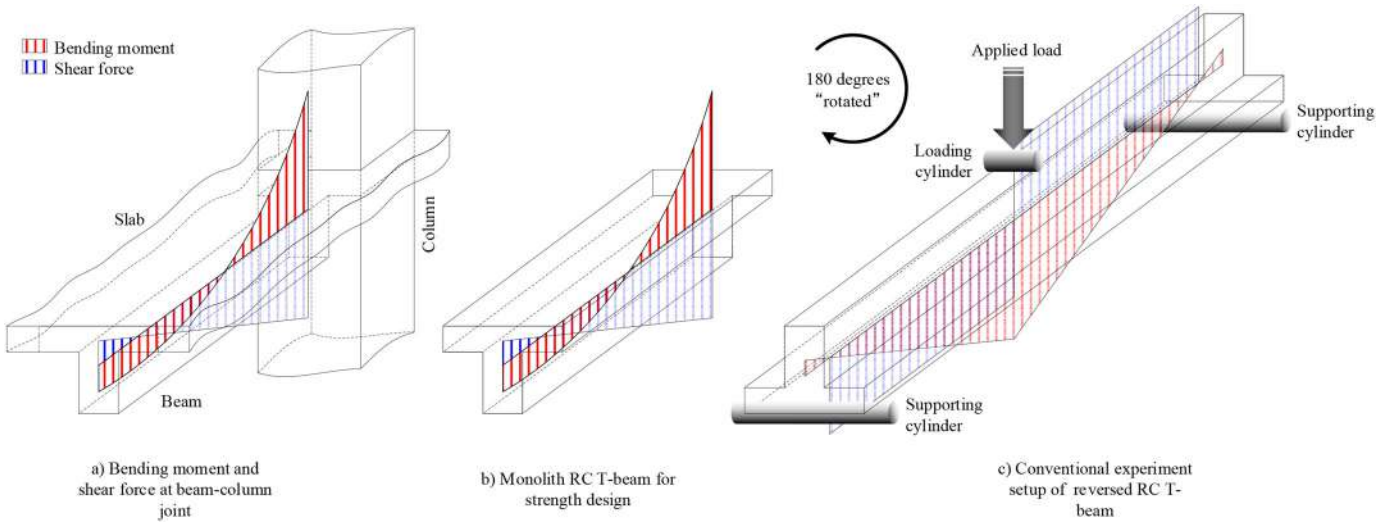

Figure 2. Scheme for bending moment and shear strengthening experiments.

was reported by Spadea et al. [14] and Tudjono et al. [15] that externally bonded CFRP sheets subjected to a combination of bending moment and shear force could significantly increase the ultimate load capacity of beams in the earthquake design. Therefore, it leads to an economic earthquake resistant design compared to separately considering bending moment and shear force design in the strengthening methods.

Although many analytical and numerical studies are available on the bending or shear strengthening of RC beams by using CFRP sheets or rods, most of those numerical investigations [16–20] on the behavior of RC beams were conducted by using finite element methods (FEMs). FEM is the most popular modeling tool used in academic institutions and industries. Moreover, FEM can model complex geometries, irregular boundary conditions, and ease of use. However, as a continuum modeling tool, FEMs cannot physically simulate concrete openings due to cracks. Moreover, the element distortions due to significant compressive stress or significant strain are the main reasons for the lacking of popularity of the FEM for modeling brittle materials, such as concrete. In the experimental investigations of CFRP strengthening RC beams under excessive loading, the stress distribution over the cross-section is complicated because of inherent material nonlinearities. This behavior highlights the importance of using nonlinear models that explicitly consider concrete tensile cracking, concrete crushing in compression, steel yielding, and CFRP tear-off behaviors.

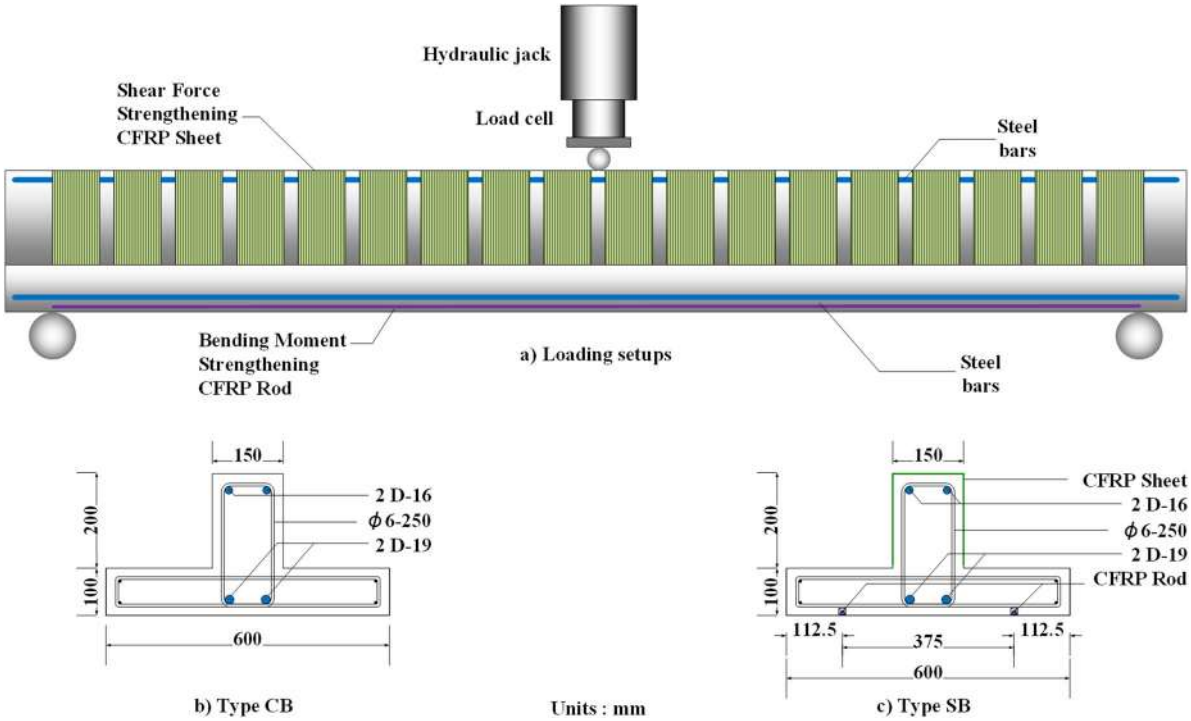

Figure 3. RC T-beam experimental setup and detailed cross-sections.

Table 1. Experimental results of the reversed RC T-beams [25].

Type of beam	P_{crack} (kN)	δ_{crack} (mm)	$P_{ultimate}$ (kN)	$\delta_{ultimate}$ (mm)
CB average	29.01	1.37	116.87	20.0
SB-1 average	49.10	1.87	155.34 (32.9%)	16.5 (−17.5%)
SB-2 average	50.20	1.70	153.38 (31.2%)	16.2 (−19.0%)

Rigid body spring model (RBSM) can simulate discrete behaviors, like steel yielding and concrete fracture, and are helpful for other engineering field applications [21–23].

Presently, the bonding mechanisms between the CFRP and concrete surface are still inconclusive and undergoing extensive research and investigations [24]. The investigation of the bond behavior is out of the scope of this work and is envisioned for further study. Therefore, a perfect bond is assumed and included in the CFRP elements.

2. Novelty of this study

The main contribution of this article is to develop RBSMs for the reversed RC T-beam strengthened with CFRP sheets and rods model and calibrate the model with experimental results from a new methodology perspective. Proper modeling techniques by using RBSM were used for simulating the nonlinear mechanical properties of concrete, reinforcing bars, and CFRP sheets and rods. A systematic calibration procedure combined with a recommendation based on the energy-based criteria to evaluate the results of calibrated load-displacement curve is proposed. Furthermore, the systematic calibration procedure proposed can be used as an essential numerical tool for designing, investigating, evaluating, and assessing the performances of CFRP strengthened RC beam structures.

3. RC T-beams tested at Diponegoro University

In this study, the experimental works which were conducted at Universitas Diponegoro [25] are referred to verify the capacity of CFRP strengthened RC T-beam by using 2D RBSM [26–29]. More detailed descriptions of these experimental works can be found in [25]. The experiments tested the unstrengthened RC T-beam (CB = Control Beam type) for comparison purposes. In the strengthened RC T-beam, strengthened beam (SB) type, the CFRP sheets were attached by wrapping the T-beam web to strengthen against the shear force, and the CFRP rods were mounted on the T-beam flange to strengthen the T-beam against the bending moment.

Figure 3(a) shows the experimental loading setup (Figure 3(a)) and detailed cross-sections of T-beams (Figure 3(b,c)). The total length of the beams was 2500 mm, and the beams were supported on their flange side by two rollers of 100 mm at both ends. The widths of the web and flange were 600 and 150 mm, respectively. The depths of the web and flange were 200 and 100 mm, respectively.

The experimental results are summarized in Table 1 and Figure 4.

Table 1 shows the CB and SB beam experimental results. Compared to that for the CB T-beam, the ultimate load of the SB beams increased by 32.9 and 31.2% for SB specimens 1 and 2, respectively. The displacement of the SB beams decreased by 17.5 and 19.0% for SB specimens 1 and 2, respectively. Therefore, the SB beams strengthened with the CFRP sheets and rods exhibited a large ductile failure mode because of the increase in the loading capacity and displacement of the CB T-beams. Figure 5 shows the tested beams' loading (P) and displacement (δ) values [25].

The curves demonstrate the effect of the strengthening of the beams. Furthermore, Figure 5 also reveals that CFRP

Figure 4. RC T-beam after the tests.

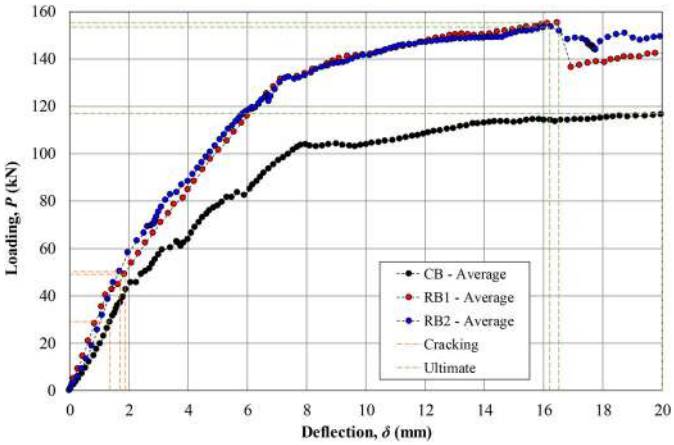

Figure 5. Load-displacements of CB and SBs experimental results.

sheets and rods strengthening increased the SB beams' loading capacity and displacement compared to the CB T-beam. A more detailed description of the experimental techniques and discussion of the results can be found in Utomo et al. [25].

4. 2D RBSM

In RBSM [26], the analytical model was discretized into polygon elements whose sides between elements are interlocked by springs. Each element had two transitional and one rotational degree of freedom at its gravity center. Normal and shear springs, attached at the boundary between two elements, were implicitly formulated using both elements' normal and shear stiffness moduli. The plane stress element represented the analysis of concrete, equivalent steel, and CFRP materials. A modified Newton–Raphson procedure was adopted to obtain the convergence. The stress and strains were computed using the stiffness matrix derived from kinematical relationships between two elements.

4.1. Plane-stress element

In RBSM, the concrete was discretized using a plane-stress polygon element (Figure 6). The interfaces of the side boundaries of the element were connected to the adjacent element by using springs in the normal and tangential directions of n and s, respectively. A description of the kinematic assumptions of the elements is shown in Figure 7.

Under the assumptions of small deformation, any arbitrary point $P(x,y)$ on the adjacent boundary between two elements can be expressed by the following:

$$\begin{aligned} U_i &= u_i - (y - y_{iG}) \cdot \theta_i \\ V_i &= v_i + (x - x_{iG}) \cdot \theta_i \end{aligned} \quad for\ i = 1,2 \tag{1}$$

where $\mathbf{U}_i = \{ U_i \quad V_i \}^T$ is the displacement vector of point P that is referenced to the center of mass of the ith element, $\mathbf{u}_i = \{ u_i \quad v_i \quad \theta_i \}^T$ is the degree of freedom vector of point P that is referenced to the center of mass of the ith element, and x_{iG}, y_{iG} are the coordinates of the center of mass of the ith element.

In the matrix form, Eq. (1) can be written as:

$$\mathbf{U}_i = \mathbf{Q}_i \cdot \mathbf{u}_i \tag{2}$$

where the matrices $\mathbf{Q}_i$ are given by:

$$\mathbf{Q}_1 = \begin{bmatrix} 1 & 0 & -(y - y_{1G}) \\ 0 & 1 & (x - x_{1G}) \end{bmatrix} \text{ and } \mathbf{Q}_2 = \begin{bmatrix} 1 & 0 & -(y - y_{2G}) \\ 0 & 1 & (x - x_{2G}) \end{bmatrix}.$$

By using coordinate transformation, the displacement of point P refers to its boundary line between elements and can be expressed by:

$$\bar{\mathbf{U}}_i = \mathbf{R} \cdot \mathbf{U}_i = \mathbf{R} \cdot \mathbf{Q}_i \cdot \mathbf{u}_i \tag{3}$$

where the coordinate transformation from global to local (n and s directions) of the matrix $\mathbf{R}$ is given by:

$$\mathbf{R} = \begin{bmatrix} \cos(n,x) & \cos(n,y) \\ \cos(s,x) & \cos(s,y) \end{bmatrix} = \begin{bmatrix} l_1 & m_1 \\ l_2 & m_2 \end{bmatrix}.$$

From Al-Mahmoud et al. [2], the total relative displacements of the point P can be expressed by:

$$\boldsymbol{\delta} = \sum_i^2 \mathbf{M}_i \cdot \bar{\mathbf{U}}_i = \sum_i^2 \mathbf{M}_i \cdot \mathbf{R} \cdot \mathbf{Q}_i \cdot \mathbf{u}_i = \sum_i^2 \mathbf{B}_i \cdot \mathbf{u}_i \tag{4}$$

where $\boldsymbol{\delta} = \{ \delta_n \quad \delta_s \}^T$ are the relative displacements of points P' and P''. The mirroring matrices $\mathbf{M}_i$ are given by:

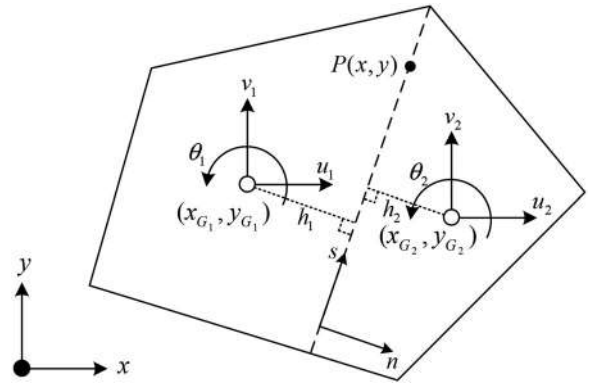

Figure 6. The displacement field of the plane-stress polygon element in RBSM.

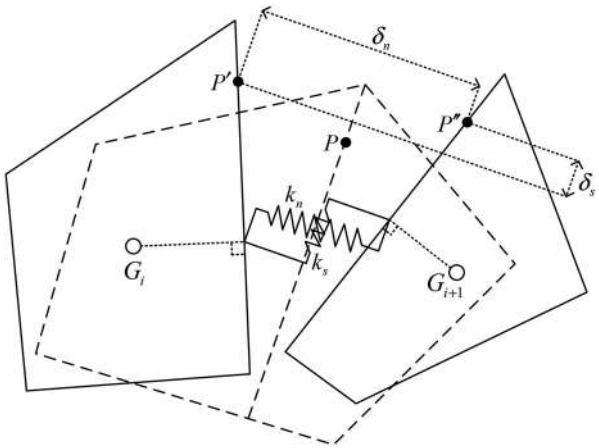

Figure 7. Kinematic description of the elements in RBSM.

$$\mathbf{M}_1 = \begin{bmatrix} -1 & 0 \\ 0 & -1 \end{bmatrix} \text{ and } \mathbf{M}_2 = \begin{bmatrix} 1 & 0 \\ 0 & 1 \end{bmatrix},$$

and the rigid body displacement matrices $\mathbf{B}_i$ are given by:

$$\mathbf{B}_1 = \begin{bmatrix} -l_1 & -m_1 & \{l_1(y-y_{1G}) - m_1(x-x_{1G})\} \\ -l_2 & -m_2 & \{l_2(y-y_{1G}) - m_2(x-x_{1G})\} \end{bmatrix}$$

and

$$\mathbf{B}_2 = \begin{bmatrix} l_1 & m_1 & \{-l_1(y-y_{2G}) + m_1(x-x_{2G})\} \\ l_2 & m_2 & \{-l_2(y-y_{2G}) + m_2(x-x_{2G})\} \end{bmatrix}.$$

In RBSM, the stress and displacement relationship of the plane stress in the concrete is expressed by:

$$\boldsymbol{\sigma} = \mathbf{D}_c \cdot \boldsymbol{\delta} \tag{5}$$

where the stress field matrix $\mathbf{D}_c$ is given by:

$$\mathbf{D}_c = \begin{bmatrix} k_n & 0 \\ 0 & k_s \end{bmatrix}.$$

The strain field vector is computed from:

$$\boldsymbol{\varepsilon} = \frac{\boldsymbol{\delta}}{h} = \frac{\boldsymbol{\delta}}{(h_1 + h_2)} \tag{6}$$

where h_1 and $h_2 (h = h_1 + h_2)$ are the normal distances in the n direction of the center of mass to the interface boundary between elements *1* and *2*, respectively. The strain field vector $\boldsymbol{\varepsilon}_c$ is given by $\boldsymbol{\varepsilon}_c = \{ \varepsilon_n \quad \gamma_s \}^T$.

From the plane stress condition, the stress and strain relationship can be written as:

$$\sigma_n = \left(\frac{E_c}{1-\nu_c^2}\right)\varepsilon_n \quad \text{and} \quad \tau_s = \left(\frac{E_c}{1+\nu_c}\right)\gamma_s. \tag{7}$$

Hence, the spring constants can be computed from:

$$k_n = \left(\frac{E_c}{1-\nu_c^2}\right)\frac{1}{h} \quad \text{and} \quad k_s = \left(\frac{E_c}{1+\nu_c}\right)\frac{1}{h}. \tag{8}$$

where E_c and ν_c are the elastic modulus and Poisson's ratio of the concrete, respectively.

4.2. Steel reinforcement bars in RBSM

In RBSM, modeling steel bars in the concrete can be implemented differently. Figure 8 shows two different implementations of steel bars in the concrete element, i.e., the steel bar is modeled using a beam/line element or an equivalent plane stress element. However, in 2D analyses, since there are no inward and outward displacements about the plane, the same results can be achieved by both types of elements when the thickness of the equivalent plane element is equal to the sectional area of the steel bars. In this study, the equivalent orthotropic plane element for the steel bars was convenient when modeling the main steel bar, stirrup, and CFRP sheet and rod elements.

4.3. Equivalent orthotropic plane element

In RBSM, the steel and CFRP material can be modeled using an equivalent thickness of orthotropic plane element with material orientation (Figure 9).

The equivalent thickness of an orthotropic plane element of steel bars and CFRP rod is formulated by,

$$\begin{pmatrix} \sigma_{x'} \\ \tau_{x'y'} \end{pmatrix} = \begin{bmatrix} E_s & 0 \\ 0 & \beta_s E_s \end{bmatrix} \begin{pmatrix} \varepsilon_{x'} \\ \gamma_{x'y'} \end{pmatrix} \tag{9}$$

In RBSM, the shear stresses in the steel and CFRP rod were considered after cracking in concrete and are known as the dowel effect [30]. Figure 10 shows the stress–strain relationship of the shear stress in the steel after the cracking of the concrete. The following shear stress equation is assumed in RBSM:

$$\tau = \beta_s E_s \gamma \tag{10}$$

where β_s and γ are the coefficients of the steel's and CFRP rod's dowel effect and dowel shear strain in cracking concrete. The coefficient β_s is given by:

$$\beta_s = \frac{3}{4}\left(\frac{d}{a_m}\right)^2 \tag{11}$$

where d and a_m are the steel bar diameter and CFRP rod diameter with the approximated cracking zone height (about $10 \sim 20$ cm).

The shear strain in the steel during the cracking of concrete γ was computed based on the slipping distance between two concrete elements upon the occurrence of a crack.

Figure 11 shows the assumed displaced plane stress element on a plane.

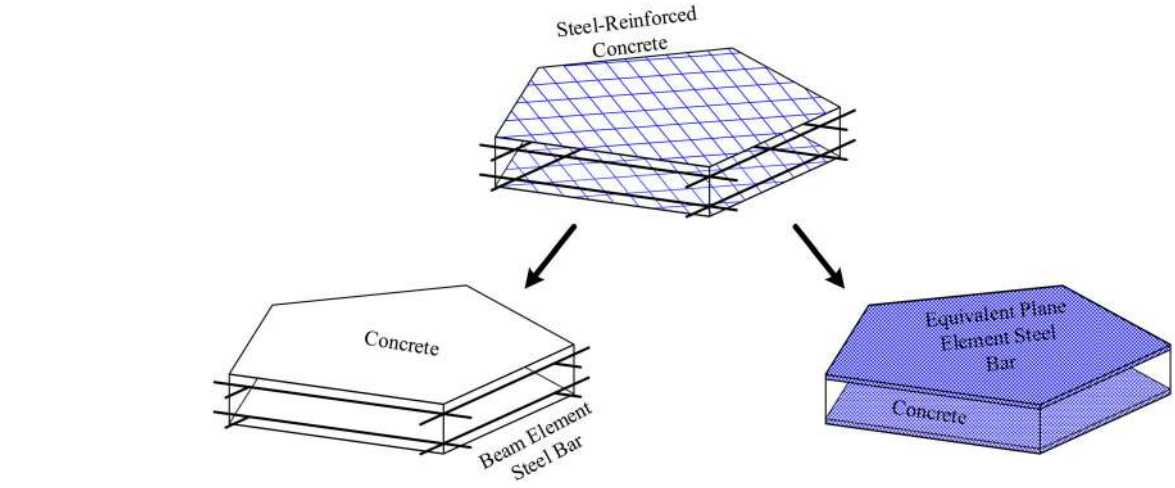

Figure 8. Steel bar reinforcement Model in RBSM.

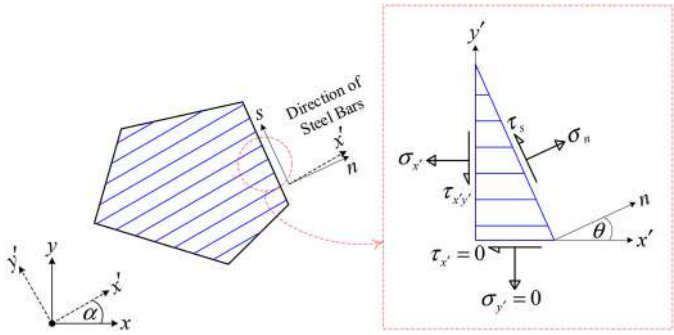

Figure 9. The orthotropic plane element and material orientation.

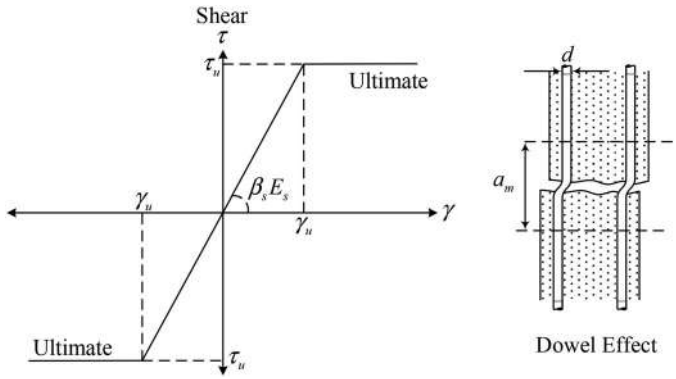

Figure 10. Shear stress modeling of steel using dowel effect at concrete cracks.

The movement of an arbitrary point P can be determined using the following strain transformation matrices from the displaced geometrical element.

$$\begin{pmatrix} \sigma_n \\ \tau_s \end{pmatrix} = \begin{bmatrix} l^2 & lm \\ -lm & l^2 \end{bmatrix} \begin{pmatrix} \sigma_{x'} \\ \tau_{x'y'} \end{pmatrix} \tag{12}$$

$$\begin{pmatrix} \delta_{x'} \\ \delta_{x'y'} \end{pmatrix} = \begin{bmatrix} l & m \\ -m & l \end{bmatrix} \begin{pmatrix} \delta_n \\ \delta_s \end{pmatrix} \tag{13}$$

$$\boldsymbol{\varepsilon} = \begin{pmatrix} \varepsilon_n \\ \varepsilon_s \end{pmatrix} = \frac{1}{h} \begin{pmatrix} \delta_n \\ \delta_s \end{pmatrix} = \frac{1}{h} \boldsymbol{\delta} \tag{14}$$

$$\boldsymbol{\varepsilon}' = \begin{pmatrix} \varepsilon_{x'} \\ \gamma_{x'y'} \end{pmatrix} = \frac{\cos\theta}{h} \begin{pmatrix} \delta_{x'} \\ \delta_{x'y'} \end{pmatrix} = \frac{\cos\theta}{h} \boldsymbol{\delta}' \tag{15}$$

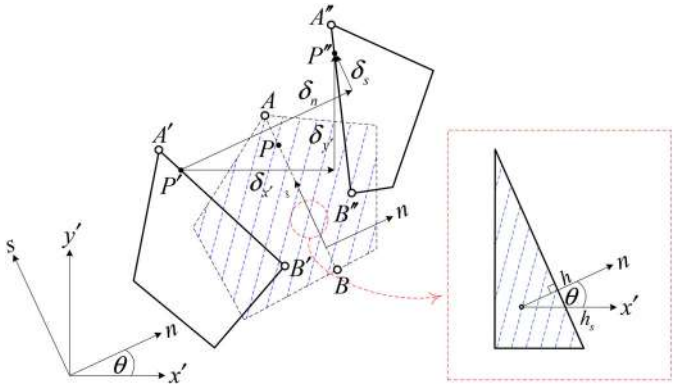

Figure 11. Kinematic of steel reinforcement and coordinate transformation.

$$\begin{pmatrix} \varepsilon_{x'} \\ \gamma_{x'y'} \end{pmatrix} = \begin{bmatrix} l^2 & lm \\ -lm & l^2 \end{bmatrix} \begin{pmatrix} \varepsilon_n \\ \gamma_s \end{pmatrix} \tag{16}$$

The steel's normal and shear strains from Eq. (14) can be calculated using Eqs. (15) and (16), where the element's global displacement vector $\boldsymbol{\delta}'$ is transformed into the element's local displacement vector $\boldsymbol{\delta}$.

The stress and displacement relationship of the orthotropic element of equivalent thickness steel bars and CFRP rod material can be given as,

$$\boldsymbol{\sigma} = \mathbf{D}_s \cdot \boldsymbol{\delta} \tag{17}$$

where,

$$\mathbf{D}_s = \frac{E_s \cos^2\theta}{h} \begin{bmatrix} \cos^2\theta + \beta_s \sin^2\theta & (\beta_s - 1)\cos\theta \sin\theta \\ (\beta_s - 1)\cos\theta \sin\theta & \sin^2\theta + \beta_s \cos^2\theta \end{bmatrix} \begin{pmatrix} \delta_n \\ \delta_s \end{pmatrix}. \tag{18}$$

4.4. Constitutive equations

Because the joint between the interface of two elements was connected with both normal and tangential distributed springs in the generalized discrete analysis of the RBSM model, the cracking, failure, shear fracture, and other failure conditions of the concrete can be directly observed.

In a tensile region of the concrete, the normal spring in the RBSM element was rolled by the uniaxial stress–strain relationship, as shown in Figure 12 on the left side of the stress-strain relationship graph. The following equation governs the constitutive equation of concrete after the tension stiffening effect:

$$\sigma_t = \left(c_1 + c_2\varepsilon + c_3\varepsilon^2 + c_4\varepsilon^3\right)F_t. \tag{19}$$

where c_1, c_2, c_3, c_4 are constants.

In the compressive region of concrete, the initial stiffness of the concrete was considered up to F_{c1}, which was presumed to be the 50% of the ultimate compression strength of the cylindrical concrete test result. F_c. F_{c1} was assumed as the occurrence of the first yielding point of the concrete. After that, the softening effect continued F_{c2}, which was presumed to be 95%F_c. Herewith, F_{c2} was assumed as the occurrence of the second yielding point of the concrete with the coefficient of modulus β used to reduce the initial elastic modulus by 50%. Beyond the second yielding point, instead of having a single peak, a plateau region where $\beta = 0$ was considered until the strain limit under compression was reached. The strain limit under compression in RBSM was considered two times the strain limit under compression $2\varepsilon_{cu}$, which was not less than the value $0.2F_c$after the limit.

In both the tensile and compressive regions of the steel material, the normal spring in the RBSM element was ruled by a uniaxial stress-strain relationship, as shown in Figure 13(a), where the stress–strain relationship is shown as symmetric and perfectly plastic yield curves. Similar to the concrete, the CFRP fibers did not have any compressive resistance, although the fibers had a stronger tensile capacity than that of the steel material. To model the CFRP material in the RBSM, the uniaxial stress-strain relationship shown in Figure 13(b) is assumed. The compressive region was presumed to have a very small modulus compared to the tensile region to avoid computational floating-point problems if the modulus was set to zero.

4.5. Failure conditions

The constitutive equations were solely determined from simple compression or tension tests. However, under complex loading conditions, a combination of normal and shear stresses impacts the elements in the model. Furthermore, the stress and strain behavior beyond the yielding point has to be expressed explicitly to consider the stress combination acting in an element.

The modified Mohr–Coulomb yield criteria were adopted to consider the combination of normal and shear stresses in the concrete and the equivalent orthotropic plane stress element of steel reinforcements. The original Mohr–Coulomb equation for shear stress is given by:

$$\tau = \sigma \tan\phi + c \tag{20}$$

where ϕ and c are the concrete's friction angle and cohesive strength, respectively.

The plastic flow of the modified Mohr–Coulomb yield criteria is shown in Figure 14.

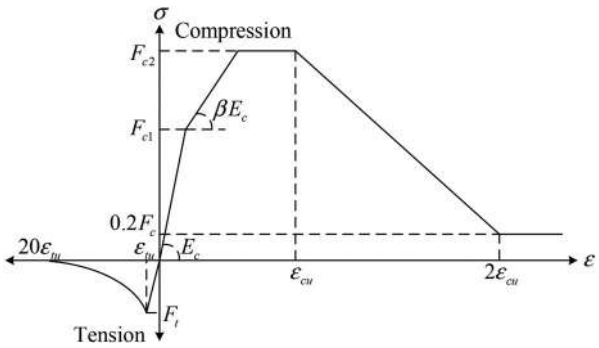

Figure 12. Stress–strain relationship of concrete material.

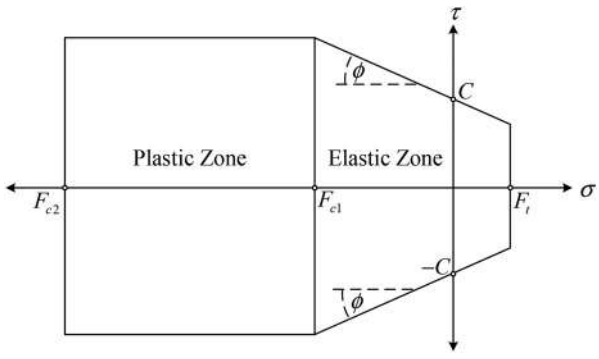

Figure 14. Modified Mohr–Coulomb yield criteria in RBSM.

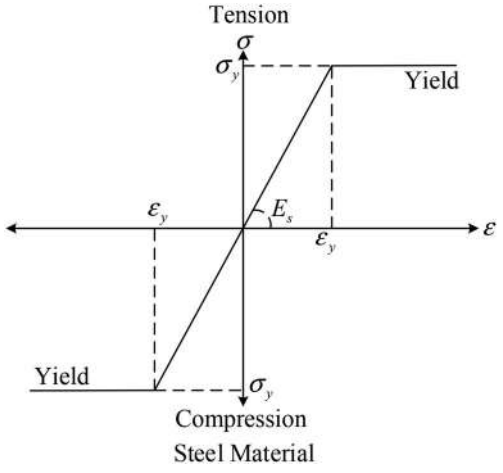

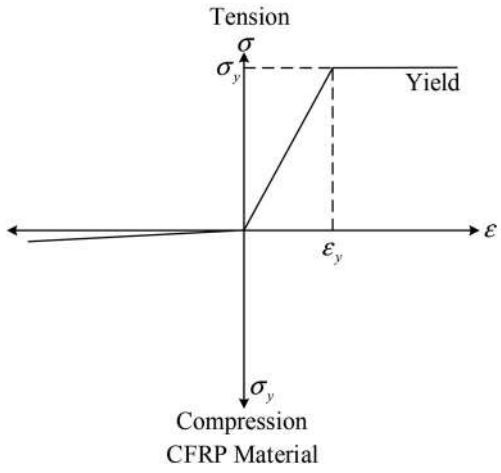

Figure 13. Stress–strain relationship of typical steel material and CFRP material.

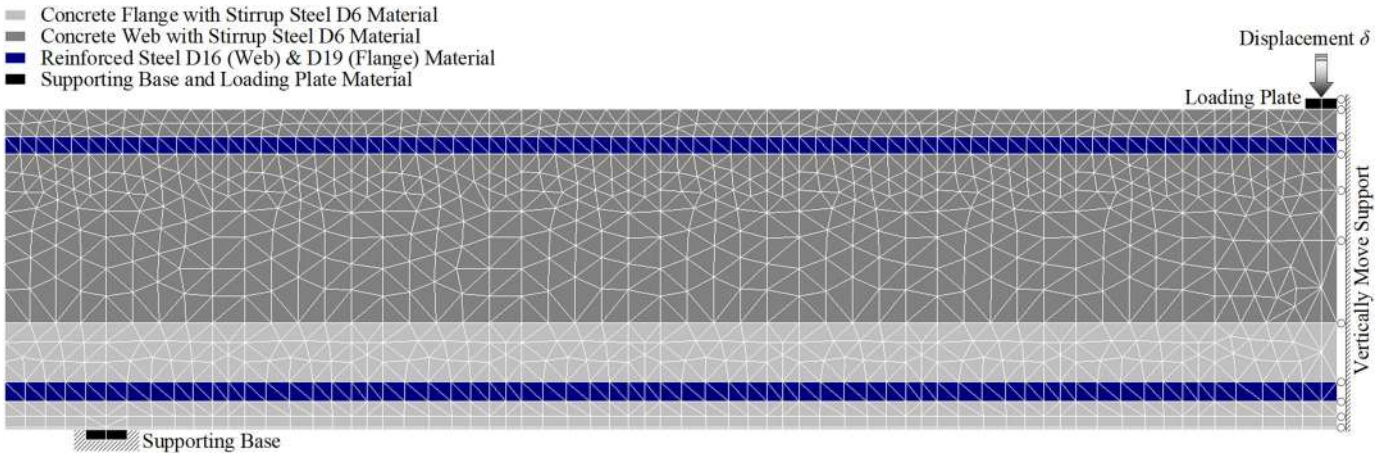

Figure 15. The symmetric half-span CB T-beam model for calibration purposes.

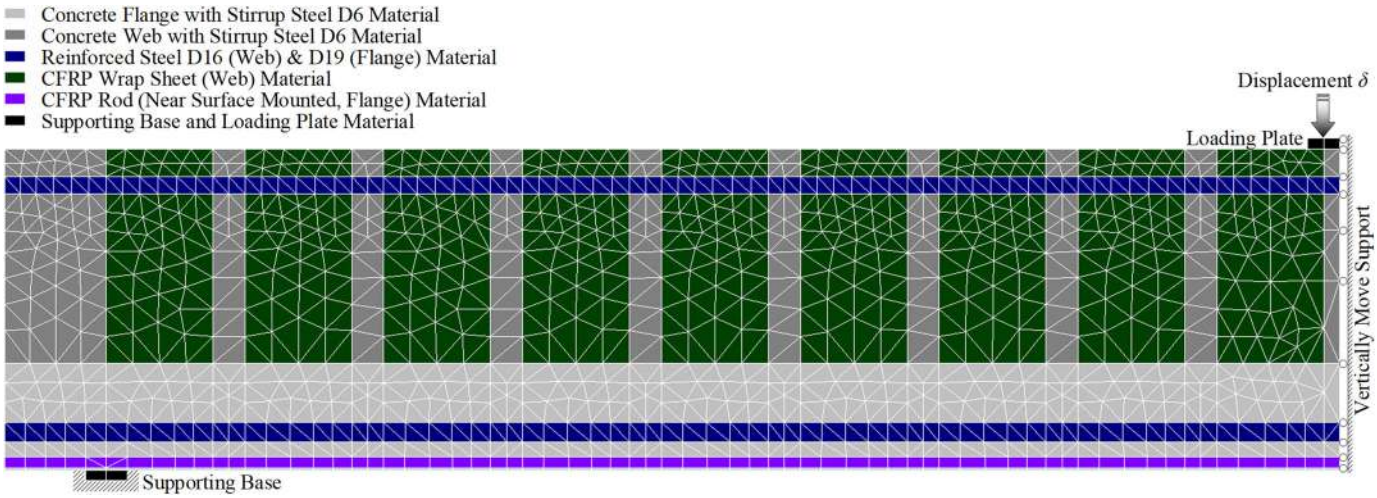

Figure 16. The symmetric half-span SB beam model for calibration purposes.

Table 2. Mechanical properties of concrete material.

Property	Min value	Max value	Source	Note
Poisson's ratio	0.167		Literature	
Cohesive strength, C [MPa]	4.90		[33]	$0.14F_c^*$
Friction angle,ϕ[degree]	37.0			
Ultimate tensile stress, F_t [MPa]	19.64			$0.8F_t^*$
Residual tensile stress coefficient, c_1	1.0526		Linear gradient line	
Residual tensile stress coefficient, c_2	−197.40		from F_t to 0	
Residual tensile stress coefficient, c_3	0.0			
Residual tensile stress coefficient, c_4	0.0			
Ultimate tensile strain,ε_{tu}	0.00533			$20\varepsilon_t$
1st Compressive gradient, E_c [MPa]	41,300		Literature [33]	$1.4E_c^*$
2nd Compressive gradient,βE_c[MPa]	20,650		Literature [26]	$\beta = 0.5$
1st Yield stress, F_{c1} [MPa]	15.84	28.90		$(50 \sim 70\%)F_c$
2nd Yield stress, F_{c2} [MPa]	30.10	39.23	Test results [25]	$95\%F_c$
Ultimate compressive strain,ε_{cu}	0.003		Literature [26]	

In RBSM, the yield function of shearing slip function f is given as:

$$f = \tau^2 + (C - \sigma \tan \phi)^2. \tag{21}$$

Based on the theory of plasticity and flow, the plastic potential energy of yield function is equal to the incremental stress as:

$$\Delta\boldsymbol{\sigma} = \left(\mathbf{D}^{(e)} - \frac{\mathbf{D}^{(e)} \frac{\partial f}{\boldsymbol{\sigma}} \frac{\partial f}{\boldsymbol{\sigma}} \mathbf{D}^{(e)}}{\frac{\partial f}{\boldsymbol{\sigma}} \mathbf{D}^{(e)} \frac{\partial f}{\boldsymbol{\sigma}}} \right) \Delta\boldsymbol{\varepsilon}. \tag{22}$$

where $\Delta\boldsymbol{\sigma}$ is the plastic incremental stress field vector of plane stress concrete element.

Table 3. Mechanical properties of steel reinforcing bars and CFRP material.

Property	Min value	Max value	Source	Note
Modulus of elasticity, E_s [MPa]	2.00E + 05 (steel bars)		Test results [25]	
	2.25E + 05 (CFRP sheet)			
	2.30E + 05 (CFRP rod)			
Yield stress, F_y [MPa]	433.54	433.75 (D19)		
	413.42	418.72 (D16)		
	670.10	738.85 (D6)		
	3700.0 (CFRP sheet)		SikaWrap-231C	Product Data Sheet
	2000.0 (CFRP rod)		SikaWrap FX-50C	PT. SIKA Indonesia
Dowel effect coefficient β_s	0.0021089 (D19)		Literature [26]	
	0.0020794 (D16)			
	0.002300 (CFRP rod)		SikaWrap FX-50C	Product Data Sheet PT. SIKA Indonesia

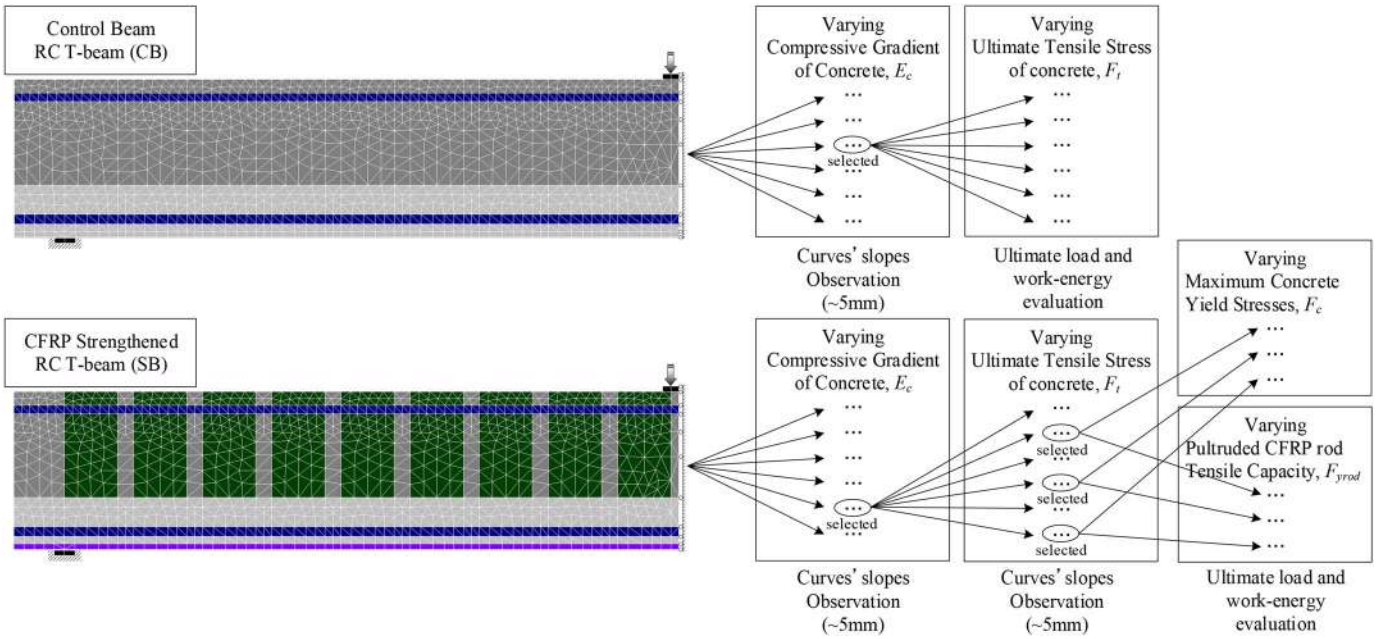

Figure 17. Calibration procedure and evaluation criteria.

Substituting [23] into [31] results in the plastic stress field matrix $\mathbf{D}_c^{(p)}$:

$$\mathbf{D}_c^{(p)} = \mathbf{D}_c^{(e)} - \mathbf{S} \tag{23}$$

with:

$$\mathbf{S} = \frac{1}{F}\begin{pmatrix} \{(C-\sigma_n \tan\phi)\tan\phi\, k_n\}^2 & \tau(C-\sigma_n\tan\phi)\tan\phi\, k_s k_n \\ \tau(C-\sigma_n\tan\phi)\tan\phi\, k_s k_n & \tau_s^2 k_s^2 \end{pmatrix}$$

$$F = \tau_s^2 k_s + \{(c-\sigma_n\tan\phi)\tan\phi\}^2 k_n$$

In the plastic zone, the unloading factor$\lambda$is given by:

$$\lambda = \frac{1}{2F}\{\tau_s k_s \Delta\gamma_s + (c-\sigma_n\tan\phi)\tan\phi\, k_n \Delta\varepsilon_n\} \tag{24}$$

4.6. Equilibrium equation

Applying the virtual work to the potential stationary, static equilibrium equation and assuming a constant thickness for the plane stress element resulted in:

$$\mathbf{F} = \int_V (\mathbf{B}^T \cdot \mathbf{D} \cdot \mathbf{B})\, dV = t\int_A (\mathbf{B}^T \cdot \mathbf{D} \cdot \mathbf{B})\, dA = \mathbf{K}\cdot\mathbf{u} \tag{25}$$

where $\mathbf{K}$ is the element stiffness matrix, which is integrated numerically, $\mathbf{u}$ is the generalized spring displacement matrix, $\mathbf{B}$ is the strain-displacement matrix that relates strain at any arbitrary point to the spring displacements of the element, t is the thickness of the element, A is the area of the element, and the material matrix $\mathbf{D}$ is given as:

$$\mathbf{D} = \mathbf{D}_c + \sum \mathbf{D}_s. \tag{26}$$

5. Calibration procedure and experimental verification

5.1. RBSM modeling

The model of RBSM was developed to represent CB and SB beams. A midspan vertical displacement was applied at the stiffened loading plate on the top of the midspan in the model. Modeling only half of the structural members took advantage of the symmetry of the problem. CB and SB models were cast for the study, shown in Figures 15 and 16, to illustrate discretization using the RBSM. The triangle plane stress element was used to model the beams' concrete, reinforcing steel bars, stirrup steel bars, and CFRP

Table 4. Input parameter of the 1st compressive gradient of concrete E_c.

Model	Ec-1	Ec-2	Ec-3	Ec-4
CB				
E_c[MPa] =	41,300	10,325	5 163	6 143
$P_{crack}[kN]$ =	15.49 (29.1)	18.17 (29.1)	21.64 (29.1)	20.64 (29.1)
$\delta_{crack}[mm]$ =	0.15 (1.37)	0.60 (1.37)	1.18 (1.37)	1.00 (1.37)
SB (averaged)				
E_c[MPa] =	6 143	8 105	9 085	12 399
$P_{crack}[kN]$ =	34.51 (29.1)	32.07 (29.1)	31.04 (49.7)	29.3 (29.1)
$\delta_{crack}[mm]$ =	1.65 (1.37)	1.26 (1.37)	1.12 (1.79)	0.83 (1.37)

Values inside the bracket show the test results by visually inspecting cracks using bare eyes.

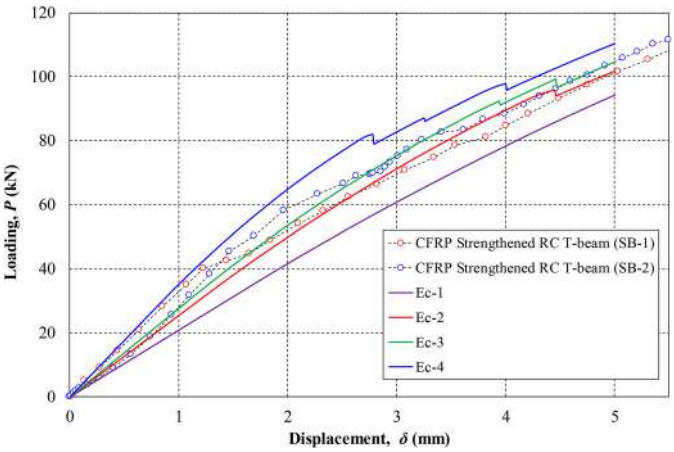

Figure 19. Calibration of test results of SB-1 and SB-2 T-beams on the E_c values.

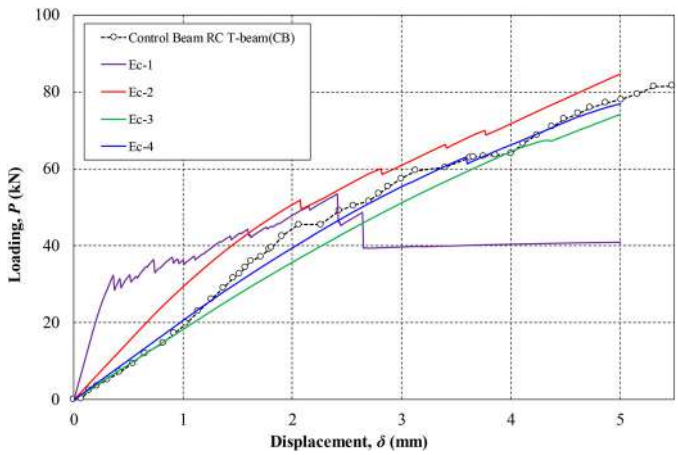

Figure 18. Calibration of test results of CB T-beams on the E_c values.

sheets and rods. Figure 15 shows the reversed RC T-beam model of CB type, and Figure 16 shows the CFRP sheets and rods strengthened the reversed RC T-beam model of SB type.

The model used in this study has 2044 plane stress triangle elements and 1166 nodes. Unlike the FEM analyses, the presumed initial crack occurrence locations were unnecessary in the model. Finding the crack occurrence locations can be done by examining the elements that had the springs in tension after yielding.

5.2. Input parameter of mechanical properties

Concrete, steel, and CFRP material test results are prerequisites for the calibration process and validation of the experimental results in RBSM analyses. The mechanical properties of steel bars and CFRPs material were obtained from tensile strength tests [25] and [31] product specification, respectively. Because the mechanical properties of concrete material available for the input parameter in RBSM are only cylindrical compressive strengths [25], the other input parameters are taken from the RBSM-specific literature [33].

The concrete material has a compressive design strength of 35 MPa (F_c^*). The mean value of the 28-d cylindrical compressive strengths of the nine specimens was 38.4 MPa [25]. The nine specimens had a standard deviation of 2.48 MPa.

The tension test of reinforcing steel bars was conducted for D6, D16, and D19 specimens to obtain the yield strengths. In the flange of the beams, the 19 mm longitudinal steel reinforcement bars had an average yield strength of 433 MPa. The 16 mm longitudinal steel reinforcement bars had an average yield strength of 416 MPa. Along with the web of the beams, the φ6 steel bars at equal intervals of 250 mm were used as stirrups. The modulus of elasticity of the steel material was assumed to be 200 GPa.

In the type SB beams, the 0.129 mm thick CFRP sheets were cut into 550 × 100 mm rectangles and bonded to the concrete compression web side of the T-beams using a base primer resin and hardener. The interval between the CFRP sheets was 30 mm. The CFRP sheet material SikaWrap-231C [31] was plied by unidirectional woven carbon fiber with an ultimate tensile strength of 3.7 GPa at 1.91% elongation tensile modulus of elasticity of 225 GPa. In addition to strengthening the CFRP sheets, using two epoxy resins, a 10 mm rod is pultruded from CFRP fiber material SikaWrap-FX50 [31]. The rods were embedded near the concrete surface of the flange. The pultruded CFRP rod has an approximated ultimate tensile strength of 2.0 GPa at 1.20% elongation that yielded with a tensile modulus of elasticity of 230 GPa.

Tables 2 and 3 show the mechanical properties of concrete, steel bar, CFRP sheet, and rod materials as the initial values used for running the RBSM models to calibrate the experimental works.

5.3. Calibration procedure and evaluation criteria

In much of the literature [2,16,32], the experimental results' calibration, verification, or validation are merely targeting the ultimate loading by using trial and error methods. In addition, the calibration of the model's behavior was usually based on the "fitness" of the load-displacement curve using

Table 5. Input parameter of the ultimate tensile stress and its residual tensile coefficients of concrete E_c.

Model	Ft-1	Ft-2	Ft-3	Ft-4	Fc-1	Fc-2	Trod-1	Trod-2
CB								
F_t[MPa] =	1.471	1.667	1.765	1.863				
c_1 =	1.0526	1.0526	1.0526	1.0526				
c_2 =	−219.8	−193.9	−183.2	−173.5				
ε_{tu} =	0.00479	0.00543	0.00575	0.00607				
SB								
F_t[MPa] =	2.550	2.942	3.236	3.530	2.942	3.236	2.942	3.236
c_1 =	1.0526	1.0526	1.0526	1.0526	1.0526	1.0526	1.0526	1.0526
c_2 =	−375.0	−375.0	−375.0	−375.0	−375.0	−375.0	−375.0	−375.0
ε_{tu} =	0.00280	0.00280	0.00280	0.00280	0.00280	0.00280	0.00280	0.00280
F_{c1}[MPa] =		161.523	161.523		195.790	195.790	161.523	161.523
F_{c2}[MPa] =		306.894	306.894		371.990	371.990	306.894	306.894
F_{y-rod}[MPa] =		1999.58	1999.58				2489.91	2489.91

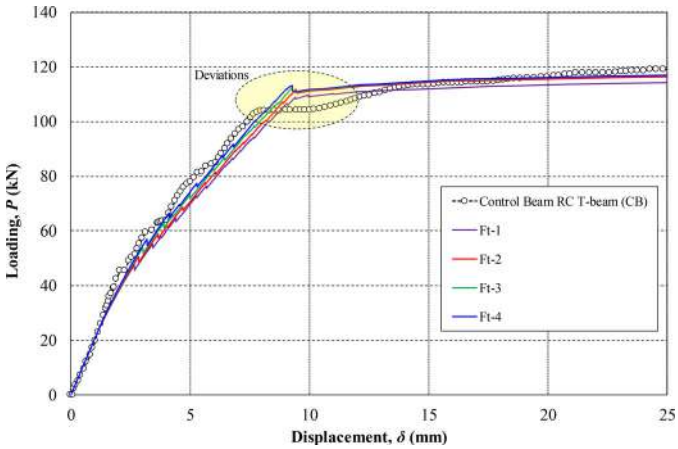

Figure 20. Load-displacements comparison of CB T-beam test and calibrations results.

bare eyes. Most of the literature does not discuss the methodology of calibrating the inherent mechanical properties in the model.

After experimentation with several trial and error efforts by using RBSM models in calibrating, the authors recommend a systematic calibration procedure that effectively predicts the load-displacement behaviors of the experimental results of CB and SB-1,2 shown in Figure 5. It is the utmost consideration that the trial value of the mechanical properties of materials should not significantly deviate from the values of experimental results or empirical formulas. Moreover, parameters, such as steel and CFRP tensile tests can be kept constant during the calibration.

Figure 17 shows a systematic calibration process that can effectively predict the behaviors of beams in the experiments numerically. In Table 1, the 1st compressive gradient of concreteE_c, plays an important role in adjusting the gradient of the load-displacement curve of the experimental results in the early stage of loading (∼5 mm). After obtaining the best prediction ofE_c, the next step is to calibrate the ultimate tensile stress of concrete,F_t. By varying the value of F_t, the decreasing gradation of the curves after the 1st yield of concrete in compressive can be achieved. In the case of SB-1,2 calibration, the variation of maximum concrete yield stresses and CFRP rod tensile capacity show some sensitivity to the load-displacement curve post the 1st yielding of concrete material.

In other works, the comparison of ultimate loads between test and numerical results is mostly adopted as a single verification criterion. In most literature, the "fitness" of the load-displacement curves prediction was usually evaluated using bare eyes (visual inspection) to compare the test and numerical results. In this study, an attempt to define a quantitative evaluation of the "fitness" of the load-displacement curves by using energy-based criteria is proposed.

Energy dissipation against earthquake loading is widely used to evaluate the earthquake strengthening effects in building and structural engineering fields. In this study, an energy-based evaluation criterion is introduced to provide a more comprehensive evaluation of the prediction results of calibrations. The energy is computed from the work done from the load-displacement curves. Thus, there are two quantitative evaluation criteria in the calibration processes.

Following the procedure described above, the subsequent sections discuss step-by-step calibration and evaluation for experimental results.

5.4. Calibration on 1st compressive gradient of concrete, E_c

After conducting several trial efforts, it was found that the gradient of the tested CB, SB1, and SB2 beams in the early stage of loading is determined by the value of 1st compressive gradient of the concrete material; hence the first attempt is to try several values starting from the values mentioned in Table 2. The other input mechanical properties are using the data given in Table 2. The average value is used whenever a parameter has a minimum and maximum value. Table 4 and Figures 18 and 19 show CB, SB-1, and SB-2 test results calibrated within 5 mm displacement.

It can be observed from Table 4 that the initiation of concrete cracking varies depending on the gradients of the 1st compressive gradient of concrete. From the best selected Ec-4 of CB T-beam and Ec-3 of SB-1,2 T-beam models, the results of numerical prediction show less load and displacement values, which show that the initiation of crackings is earlier than the test results. The reason is that the tests' cracks detection was conducted by visual inspection using bare eyes, which is inaccurate.

In Figure 18, the best fitness to CB test result was found that 6143 MPa of the 1st gradient compressive strength agrees with the test results. This value is much lower than the cylindrical test results. Similarly, in Figure 19, the best fitness to SB-1,2 test results was found that 9085 MPa of the

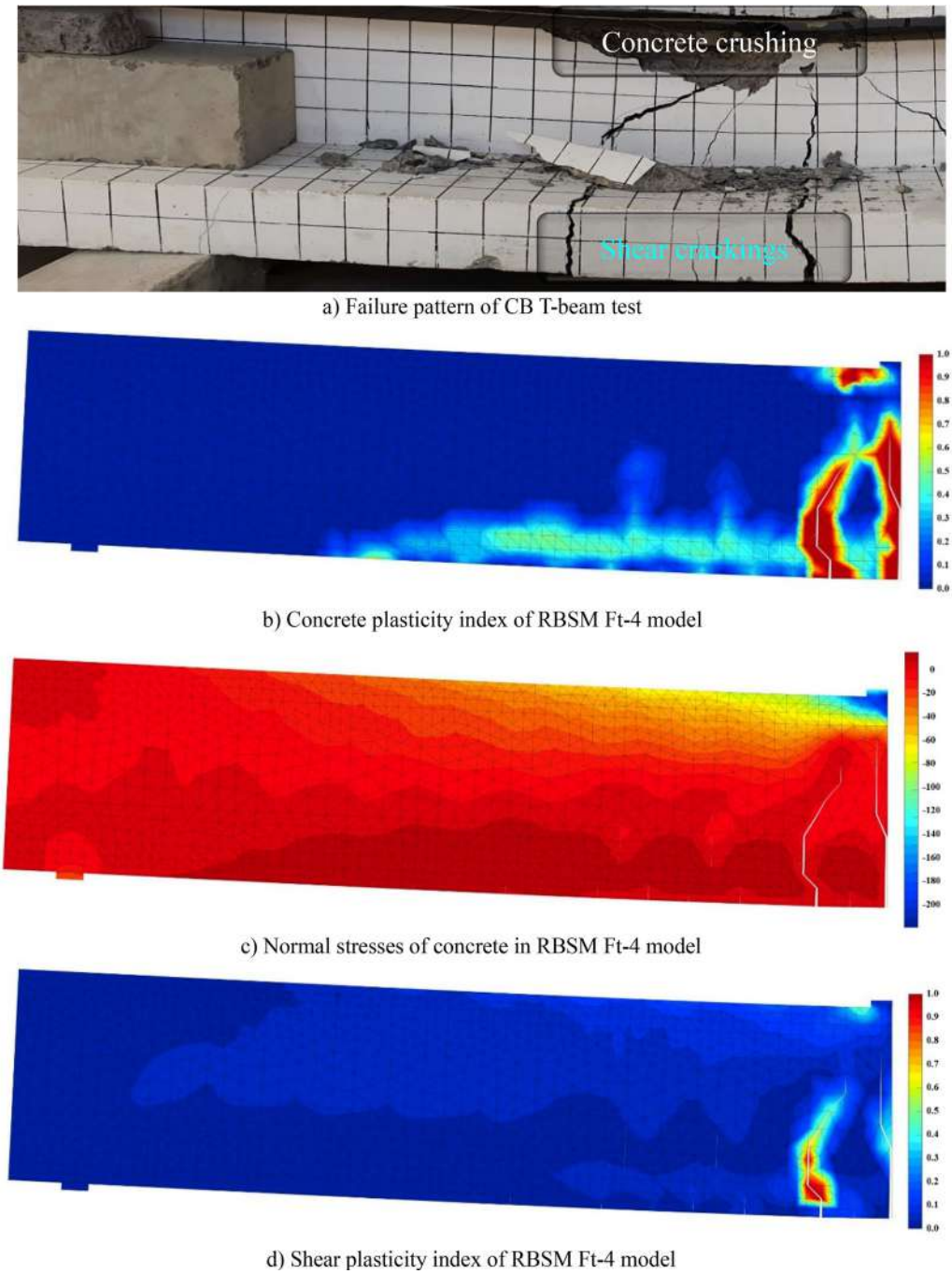

Figure 21. Comparisons of failure patterns and stress conditions between the test and calibration results of CB T-beam at the ultimate load.

1st gradient compressive strength also agrees with the test results. This value is also lower than the cylindrical test results. Both values are lower than the test results because the 1st gradient of compressive strength obtained from the cylindrical test results was obtained from concrete material's pure axial loading test. However, when the concrete material is subjected to the bending moment, lower gradient compressive strength can result because the crack openings propagate to reduce the cross-section of the beams. Comparing both calibrated results, CB's 1st gradient of compressive strength is lower than the SB-1,2 because the confinement and tension strengthening effects due to the CFRP sheets and rods are expected.

5.5. Calibration on ultimate tensile stress of concrete, F_t

From the results in the previous section, Ec-4 from the CB T-beams calibration and Ec-3 from the SB-1,2 T-beams calibration are selected as bases for the following calibration process. After conducting several trial efforts, it was found that the changing of load-displacement curves beyond 5 mm of the tested CB, SB-1,2 T-beams after the 1st yield of the concrete part is determined by the value of the ultimate tensile stress and its residual tensile stress coefficients of the concrete material, trial values starting from the values shown in Table 2. Table 5 and Figures 20 and 21 show CB, SB-1, and SB-2 test results, further calibrated after 5 mm displacement by

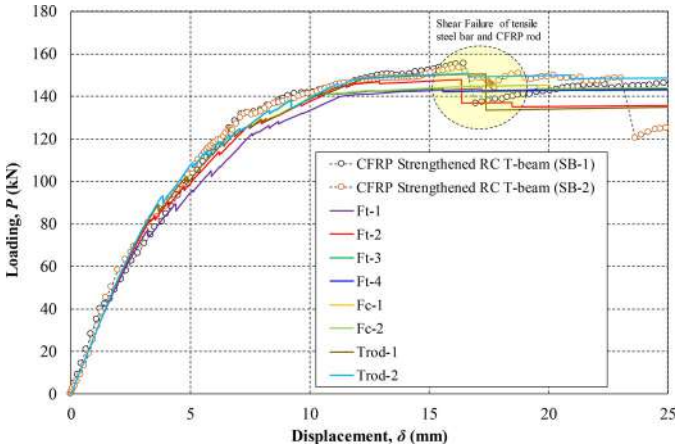

Figure 22. Load-displacements comparison of SB-1,2 T-beam test and calibrations results.

varying the ultimate tensile stress and its residual tensile stress coefficients. In addition, in the SB-1,2 cases where the CFRP rod was made by pultruding the CFRP fiber/string by using bond, the rod cross-section was not entirely composed of fiber/string; hence the CFRP rod was subjected to calibration. Table 5 and Figures 20 and 21 show the CB failure pattern of test and calibration results. Figures 22 and 23 show the representative SB-1 failure patterns of test and calibration results.

In Figure 20, the calibrated CB T-beams load-displacement curves depict some discrepancies near the 1st yielding point of concrete in compression initiated by crushing the concrete near the loading plate. These uncommon deviations can only be modeled using the hardening steel material after yielding. However, after observing the steel stress and strain at the loading state, all the steel materials are still within the elastic range (0.4 of plasticity index); hence it can be considered due to measurement defects during the manual operation hand-operated hydraulic jack device to increase loading.

In Figure 22, the calibrated SB-1,2 T-beams load-displacement curves show some drops in the load-displacement path. The test and calibration results indicated these drops by the shearing failure of tensile steel D19, CFRP sheet covered concrete rupture (concrete cover separation debonding due to flexural cracks) on the web, and CFRP rod cut out on the flange. This shearing failure is due to an extensive crack propagation that cannot be prevented by steel and CFRP materials.

5.6. Quantitative evaluation of the calibration results

From the calibrated results in the previous section, the ratio of ultimate loads and cumulative works (energy dissipations) are compared to the test results of CB, SB-1,2 T-beams and combined by using the square root of the sum of the squares (SRSS) method to evaluate the total "fitness" to the load-displacement curves. Table 6 and Figures 24 and 25 show the quantitative evaluations of CB, SB-1, and SB-2 calibrations compared to test results.

Figure 24(a) shows the cumulative work calculated from the load-displacement curves of calibration and test results of CB T-beams. Figure 24(b) depicts the total evaluation of "fitness" of calibration results (Ft-1,4, shown in blue) to the test result (in red). The calibration models of Ft-3 and Ft-4 show a close agreement with the test results with 1.9% of the SRSS value. The smaller value of SRSS, the best "fitness" calibration in predicting the test results of CB T-beams.

Figure 25(a) shows the cumulative work calculated from the load-displacement curves of calibration and test results of SB-1,2 T-beams (averaged). Figure 25(b) depicts the total evaluation of "fitness" of calibration results (Ft-1,4; Fc-1,2; Trod-1,2, shown in blue) to the test result (in red). The calibration models of Trod-2 have the smallest value of SRSS of 2.9%, which shows a close agreement with the test results.

It is worth noting that before quantitatively evaluating the calibration models, the best models of CB and SB-1,2 decided by visual inspection are Ft-4 and Trod-1 (Table 5). However, Table 6 and Figures 24(b) and 25(b) show that Ft-3,4 and Trod-2 lead to the smallest SRSS values, implying the best "fitness" calibrations are obtained by quantifying the evaluations.

6. Summary

The calibration processes can be summarized as follows,

- Calibration to the 1st compressive gradient of concrete material effectively fits the RBSM model with the test results in the early loading stage.
- Next, select the best calibration RBSM model using visual inspection to further calibrate the ultimate tensile stress properties for the rest of the loading stage until it reaches its ultimate loading state.
- Next, varying the best selected RBSM on the yield stress of concrete and CFRP rod yield stress properties.
- Finally, to find the best calibrated RBSM models, the ratio of ultimate strength and work done by the loading are combined using SRSS for evaluations. The smallest value of quantitative evaluation shows the best "fitness" of the load-displacement curve.

The proposed calibration procedure uses two evaluation criteria, the ratio of ultimate loads and works, to evaluate the calibration results quantitatively. The 1.9% CB T-beam RBSM model and 2.9% SB-1,2 T-beams RBSM model evaluation scores agree well with the test results.

7. Conclusions

This article proposes a systematic calibration procedure for CFRPs strengthened RC T-beams by using RBSM. The calibrated results show a good agreement with previous experimental data.

The stresses in CFRP sheets and rods at the beams' ultimate loads are within the elastic range. Hence, the debonding mechanism of CFRP composites observed in the experiments and RBSM modeling can be categorized as concrete cover separation debonding due to the bending moment (peel-off of the concrete cover) after the beams' failure by flexural cracks. The bond used in these

a) Failure pattern of SB-1 T-beam test

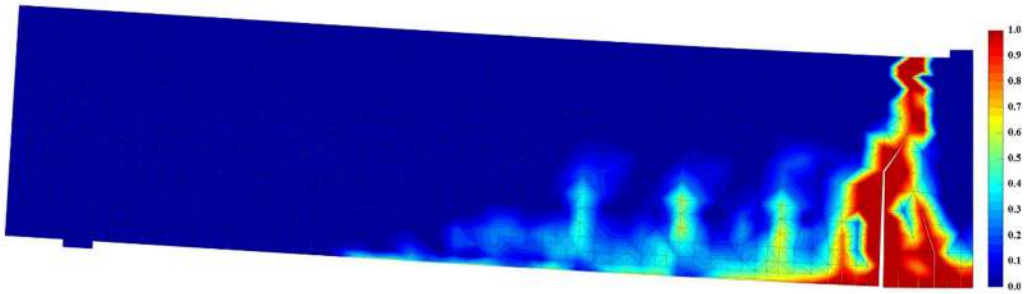

b) Concrete plasticity index of RBSM Trod-1 model

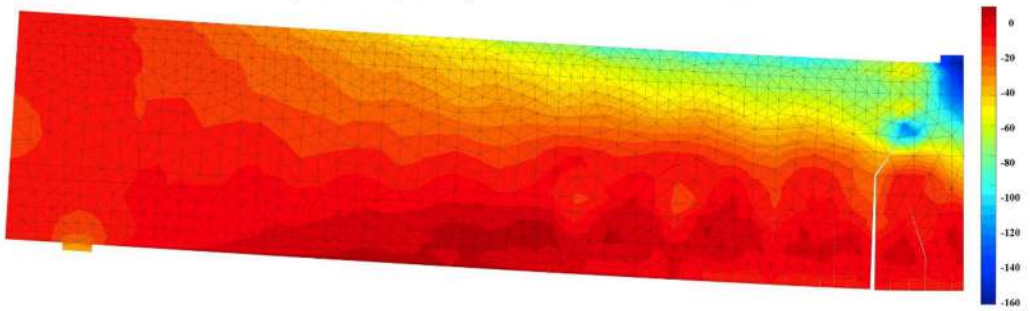

c) Normal stresses of concrete in RBSM Trod-1 model

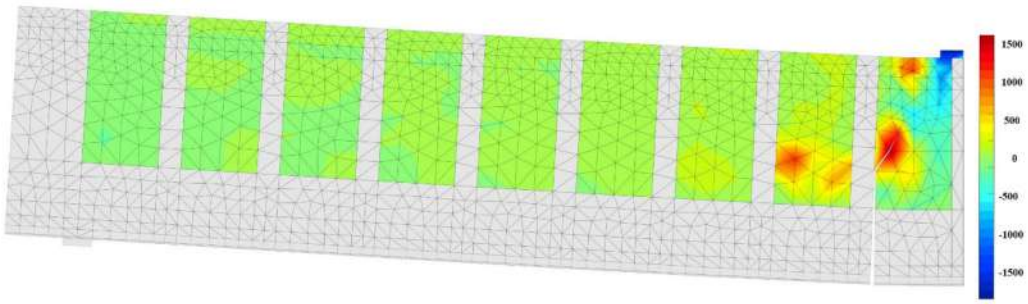

d) Normal stresses of CFRP Sheet in RBSM Trod-1 model

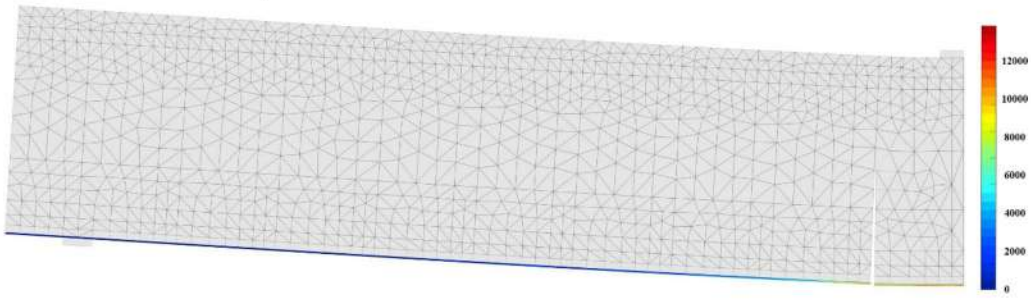

e) Normal stresses of CFRP Rod in RBSM Trod-1 model

Figure 23. Comparisons of failure patterns and stress conditions between the test and calibration results of SB-1 T-beam at the ultimate load.

Table 6. Quantitative evaluation of the calibrated CB and SB-1,2 T-beams.

Model	Ft-1	Ft-2	Ft-3	Ft-4	Fc-1	Fc-2	Trod-1	Trod-2
CB								
W [Joule] =	2 353	2 398	2 416	2 427				
W_{test} [Joule] =	2 430	2 430	2 430	2 430				
W/W_{test} [%] =	96.86	98.68	99.45	99.93				
P_u [kN] =	114.25	116.38	116.97	116.95				
P_{u-test} [kN] =	119.15	119.15	119.15	119.15				
P_u/P_{u-test} [%] =	95.89	97.67	98.16	98.15				
$SRSS$ [%] =	5.2	2.7	1.9	1.9				
SB								
W [Joule] =	3 003	3 007	3 059	3 078	3 076	3 035	3 092	3 166
W_{test} [Joule] =	3 145	3 145	3 145	3 145	3 145	3 145	3 145	3 145
W/W_{test} [%] =	95.49	95.63	97.27	97.89	97.83	96.52	98.32	100.68
P_u [kN] =	142.98	135.69	143.11	143.34	144.01	134.89	144.08	148.60
P_{u-test} [kN] =	152.92	152.92	152.92	152.92	152.92	152.92	152.92	152.92
P_u/P_{u-test} [%] =	93.50	88.73	93.59	93.74	94.17	88.21	94.22	97.18
$SRSS$ [%] =	7.9	12.1	7.0	6.6	6.2	12.3	6.0	2.9

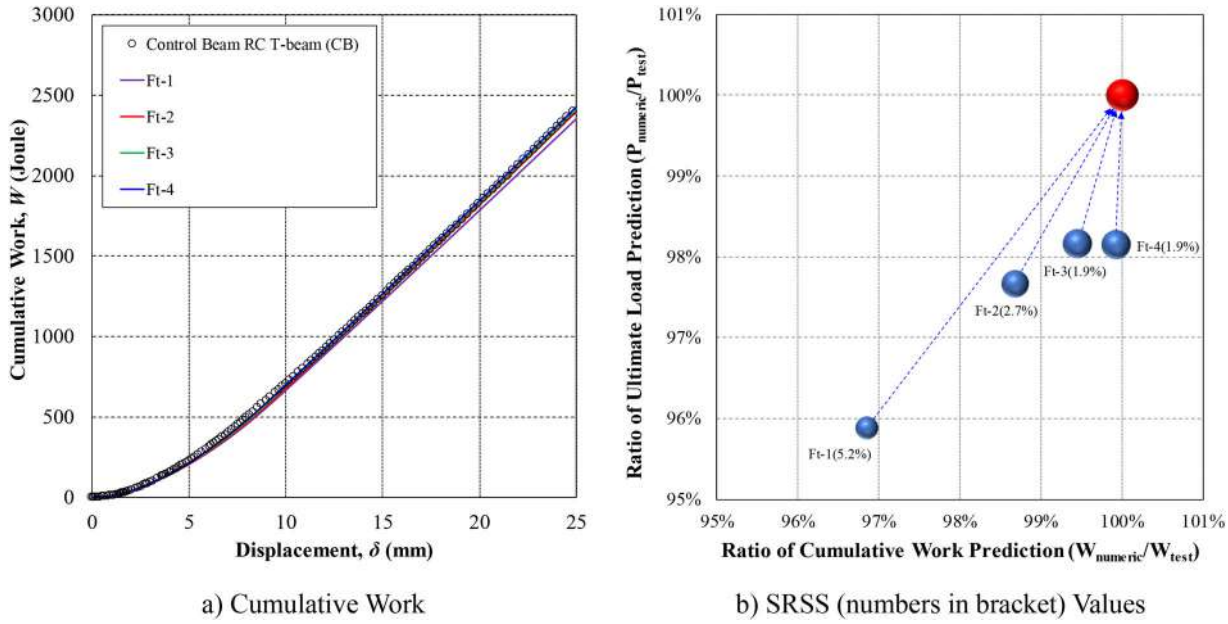

a) Cumulative Work b) SRSS (numbers in bracket) Values

Figure 24. Energy dissipation and ultimate load quantitative "fitness" evaluation of C BT-beams.

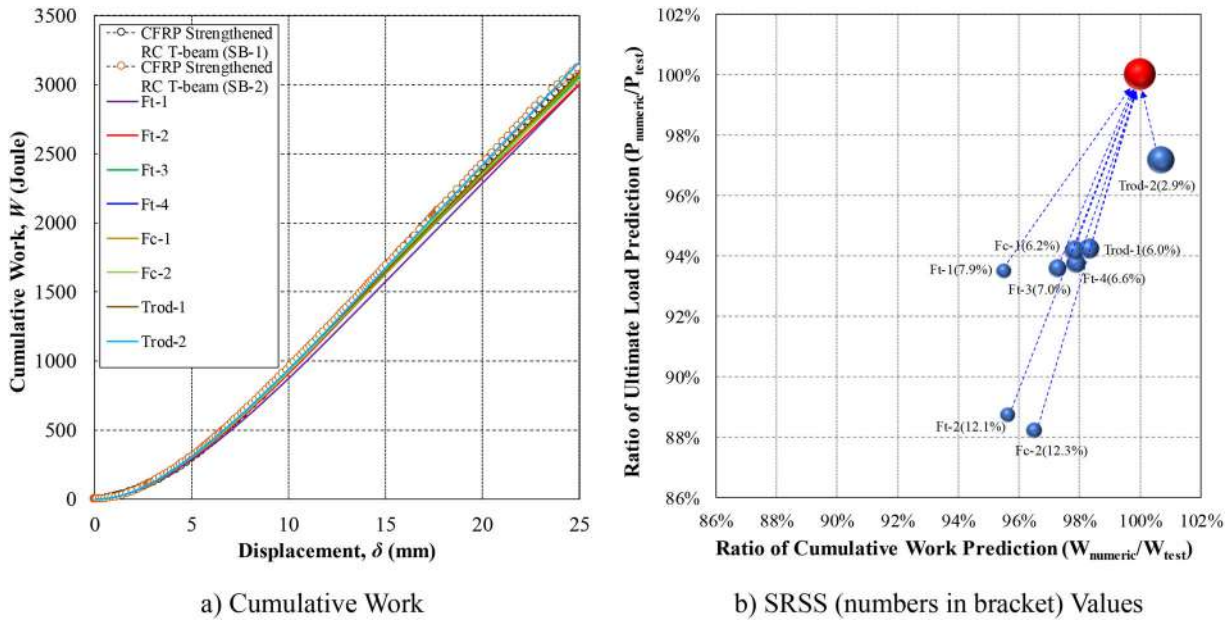

a) Cumulative Work b) SRSS (numbers in bracket) Values

Figure 25. Energy and ultimate load comparison of parametric SB-1,2 T-beams test and analyses.

experiments was also strong to peel off the concrete cover. Hence, the debonding occurred after the failure of beams. Therefore, the debonding does not affect the overall behavior of beams before the ultimate load state. However, the debonding rapidly decreases the beams' strength capacities, not affecting the evaluation criteria proposed in this study. It can be concluded that the use of fixed bonds in RBSM models proposed by this study is appropriate.

The systematic calibration procedure proposed can be used as an essential tool for designing, investigating, evaluating, and assessing the performances of CFRP strengthened RC beam structures.

An automated iterative procedure for RBSM model calibration can be envisioned for future studies by quantifying the evaluation by numbers.

Funding

This research was conducted with the support of the Diponegoro University, the World Class Research funding through the decreed No. 11-20/UN7.6.1/PP/2021.

ORCID

Joko Purnomo http://orcid.org/0000-0002-9423-5550
Aylie Han http://orcid.org/0000-0002-0990-5274
Buntara S. Gan http://orcid.org/0000-0003-1740-8363

References

[1] E. Ahmed, H. R. Sobuz, and N. M. Sutan, Flexural performance of CFRP strengthened RC beams with different degrees of strengthening schemes, Int. J. Phys. Sci., vol. 6, pp. 2229–2238, 2011. DOI: 10.5897/IJPS11.304.

[2] F. Al-Mahmoud, A. Castel, R. François, and C. Tourneur, RC beams strengthened with NSM CFRP rods and modeling of peeling-off failure, Compos. Struct., vol. 92, no. 8, pp. 1920–1930, 2010. DOI: 10.1016/j.compstruct.2010.01.002.

[3] R. Al-Rousan, A. Ababneh, and M. Alhassan, Hybrid CFRP-steel for enhancing the flexural behavior of reinforced concrete beams, J. King Saud Univ. Eng. Sci., vol. 33, no. 7, pp. 459–470, 2021. DOI: 10.1016/j.jksues.2020.06.004.

[4] A. R. Jawdhari, 2016. Behavior of RC Beams Strengthened in Flexure with Spliced CFRP Rod Panels, Ph.D. dissertation, University of Kentucky, Lexington, KY.

[5] M. M. A. Kadhim, A. Jawdhari, and A. Peiris, Evaluation of lap-splices in NSM FRP rods for retrofitting RC members, Structures, vol. 30, pp. 877–894, 2021. DOI: 10.1016/j.istruc.2021.01.054.

[6] H. Rahimi, and A. Hutchinson, Concrete beams strengthened with externally bonded FRP plates, J. Compos. Constr., vol. 5, no. 1, pp. 44–56, 2001. DOI: 10.1061/(ASCE)1090-0268(2001)5:1(44).

[7] K. Soudki, A. K. El-Sayed, and T. Vanzwol, Strengthening of concrete slab-column connections using CFRP strips, J. King Saud Univ. Eng. Sci., vol. 24, no. 1, pp. 25–33, 2012. DOI: 10.1016/j.jksues.2011.07.001.

[8] T. C. Triantafillou, and N. Plevris, Strengthening of RC beams with epoxy-bonded fibre-composite materials, Mater. Struct., vol. 25, no. 4, pp. 201–211, 1992. DOI: 10.1007/BF02473064.

[9] Tudjono, S. Ay Lie, H. L. Hidayat, and A. Purwanto, Experimental study on the concrete surface preparation ifluence to the tensile and shear bond strength of synthetic wraps, Proc. Eng., vol. 171, pp. 1116–1122, 2017. DOI: 10.1016/j.proeng.2017.01.470.

[10] D. Dutta, A. Jawdhari, and A. Fam, A new studded precast concrete sandwich wall with embedded glass-fiber-reinforced polymer channel sections: part 1, experimental study, PCI J., vol. 65, no. 3, pp. 78–99, 2020.

[11] A. El Refai, F. Abed, and A. Al-Rahmani, Structural performance and serviceability of concrete beams reinforced with hybrid (GFRP and steel) bars, Constr. Build. Mater., vol. 96, pp. 518–529, 2015. DOI: 10.1016/j.conbuildmat.2015.08.063.

[12] K. K. Tran, H. Nakamura, K. Kawamura, and M. Kunieda, Analysis of crack propagation due to rebar corrosion using RBSM, Cem. Concr. Compos., vol. 33, no. 9, pp. 906–917, 2011. DOI: 10.1016/j.cemconcomp.2011.06.001.

[13] S. Tudjono, H. A. Lie, and B. S. Gan, An integrated system for enhancing flexural members' capacity via combinations of the fiber-reinforced plastic use, retrofitting, and surface treatment techniques, Int. J. Technol., vol. 9, no. 1, pp. 5–15, 2018. DOI: 10.14716/ijtech.v9i1.298.

[14] G. Spadea, F. Bencardino, F. Sorrenti, and R. N. Swamy, Structural effectiveness of FRP materials in strengthening RC beams, Eng. Struct., vol. 99, pp. 631–641, 2015. DOI: 10.1016/j.engstruct.2015.05.021.

[15] S. Tudjono, H. A. Lie, and B. A. Hidayat, An experimental study to the influence of fiber reinforced polymer (FRP) confinement on beams subjected to bending and shear, Proc. Eng., vol. 125, pp. 1070–1075, 2015. DOI: 10.1016/j.proeng.2015.11.164.

[16] G. Camata, E. Spacone, and R. Zarnic, Experimental and nonlinear finite element studies of RC beams strengthened with FRP plates, Compos. B Eng., vol. 38, no. 2, pp. 277–288, 2007. DOI: 10.1016/j.compositesb.2005.12.003.

[17] Y. Haryanto, et al., Negative moment region flexural strengthening system of RC T-beams with half-embedded NSM FRP rods: a parametric analytical approach, J. Chin. Inst. Eng. Trans. Chin. Inst. Eng. A., vol. 44, no. 6, pp. 553–561, 2021a. DOI: 10.1080/02533839.2021.1936646.

[18] Y. Haryanto, et al., Nonlinear 3D model of double shear lap tests for the bond of near-surface mounted FRP rods in concrete considering different embedment depths, Period. Polytech. Civ. Eng., vol. 65, pp. 878–889, 2021b. DOI: 10.3311/PPci.17309.

[19] Y. Haryanto, H. T. Hu, A. L. Han, F. P. Hsiao, N. G. Wariyatno, and B. A. Hidayat, Numerical parametric study on the flexural capacity of reinforced concrete, J. Eng. Sci. Technol., vol. 16, pp. 3295–3311, 2021c.

[20] Z. J. Yang, J. F. Chen, and D. Proverbs, Finite element modelling of concrete cover separation failure in FRP plated RC beams, Constr. Build. Mater., vol. 17, no. 1, pp. 3–13, 2003. DOI: 10.1016/S0950-0618(02)00090-9.

[21] K. Farah, and Y. Sato, Numerical investigation of tension behavior of reinforced concrete members strengthened with, FRP Sheets, vol. 55, pp. 1085–1093, 2009.

[22] Y. Khmurovska, P. Štemberk, and V. Křistek, Rigid-body-spring model numerical analysis of joint performance of engineered cementitious composites and concrete, IOP Conf. Ser. Mater. Sci. Eng., vol. 246, pp. 012041–012046, 2017. DOI: 10.1088/1757-899X/246/1/012041.

[23] K. Nagai, Y. Sato, and T. Ueda, Mesoscopic simulation of failure of mortar and concrete by 3D RBSM, J. Adv. Concrete Technol., vol. 3, no. 3, pp. 385–402, 2005. DOI: 10.3151/jact.3.385.

[24] A. Jawdhari, A. Semendary, A. Fam, and I. Khoury, Bond characteristics of CFRP rod panels adhered to concrete under bending effects, J. Comp. Const., vol. 23, pp. 1, 2019.

[25] J. Utomo, N. Rabbani, S. Tudjono, and H. Aylie, The influence of external CFRP string reinforcement on the behavior of flexural RC elements, J. Geosci. Eng. Environ. Technol., vol. 6, pp. 141–146, 2021. DOI: 10.25299/jgeet.2021.6.3.5685.

[26] Takeuchi, N., (ed.), et al., 2005. Discretized limit analysis method for reinforced concrete structures. Computational Mechanic Lecture Series 7, Maruzen, Tokyo, Japan (in Japanese).

[27] T. Kawai, New element models in discrete structural analysis, J. Soc. Nav. Archit. Japan, vol. 141, pp. 187–193, 1977.
[28] T. Kawai, and N. Takeuchi, 1990. Discrete Limit Analysis Program, Series of Limit Analysis by Computer 2, Baifukan, Tokyo, Japan (in Japanese).
[29] K. Nagai, S. Yasuhiko, and T. Ueda, Mesoscopic simulation of failure of mortar and concrete by 2D RBSM, J. Adv. Concrete Technol., vol. 2, no. 3, pp. 359–374, 2004. DOI: 10.3151/jact.2.359.
[30] I. Jeli, M. N. Pavlović, and M. D. Kotsovos, A study of dowel action in reinforced concrete beams, Mag. Concr. Res., vol. 51, no. 2, pp. 131–141, 1999. DOI: 10.1680/macr.1999.51.2.131.
[31] PT. Sika Indonesia, SikaWrap-231C@ and SikaWrap-FX-50C@ Product Data Sheets, 2017. https://idn.sika.com/in/documents-resources/pds.html.
[32] T. H. Almusallam, H. Elsanadedy, Y. A. Al-Salloum, and S. H. Alsayed, Experimental and numerical investigation for the flexural strengthening of RC beams using near-surface mounted steel or GFRP bars, Const. Build. Mater., vol. 40, pp. 145–161, 2013. DOI: 10.1016/j.conbuildmat.2012.09.107.
[33] Y. Yamamoto, H. Nakamura, I. Kuroda and N. Furuya, Compression failure analysis of concrete specimens using 3D RBSM, J. Soc. Civ. Eng. Japan, vol. 64, pp. 612–630, 2008. DOI: 10.2208/jsceje.64.612.